

Influence of strain on anisotropic thermoelectric transport of Bi_2Te_3 and Sb_2Te_3

N. F. Hinsche,^{1,*} B. Yu. Yavorsky,¹ I. Mertig,^{1,2} and P. Zahn¹

¹*Institut für Physik, Martin-Luther-Universität Halle-Wittenberg, D-06099 Halle, Germany*

²*Max-Planck-Institut für Mikrostrukturphysik, Weinberg 2, D-06120 Halle, Germany*

(Dated: April 3, 2024)

On the basis of detailed first-principles calculations and semi-classical Boltzmann transport, the anisotropic thermoelectric transport properties of Bi_2Te_3 and Sb_2Te_3 under strain were investigated. It was found that due to compensation effects of the strain dependent thermopower and electrical conductivity, the related powerfactor will decrease under applied in-plane strain for Bi_2Te_3 , while being stable for Sb_2Te_3 . A clear preference for thermoelectric transport under hole-doping, as well as for the in-plane transport direction was found for both tellurides. In contrast to the electrical conductivity anisotropy, the anisotropy of the thermopower was almost robust under applied strain. The assumption of an anisotropic relaxation time for Bi_2Te_3 suggests, that already in the single crystalline system strong anisotropic scattering effects should play a role.

PACS numbers: 31.15.A-, 71.15.Mb, 72.20.Pa, 72.20.-i

I. INTRODUCTION

Thermoelectric (TE) materials are used as solid state energy devices which convert waste heat into electricity or electrical power directly into cooling or heating^{1–3}. Telluride based thermoelectrics, e.g. the bulk materials bismuth (Bi_2Te_3) and antimony telluride (Sb_2Te_3) and their related alloys, dominate efficient TE energy conversion at room temperature for the last 60 years^{4,5}. The materials TE efficiency is quantified by the figure of merit

$$ZT = \frac{\sigma S^2}{\kappa_{el} + \kappa_{ph}} T, \quad (1)$$

where σ is the electrical conductivity, S the thermopower, κ_{el} and κ_{ph} are the electronic and phononic contribution to the thermal conductivity, respectively. From Eq. 1 it is obvious, that a higher ZT is obtained by decreasing the denominator or by increasing the numerator, the latter being called powerfactor $\text{PF} = \sigma S^2$. While bulk Bi_2Te_3 and Sb_2Te_3 show ZT values smaller 1 and applications have been limited to niche areas, a break-through experiment of Venkatasubramanian *et al.* showed a remarkable $ZT = 2.4/1.5$ for p-type/n-type superlattices (SL) composed of the two bulk tellurides^{5–7}. With the availability of high- ZT materials, many new applications will emerge². The idea of thermoelectric SL follows the idea of phonon-blocking and electron-transmitting at the same time. It suggests that cross-plane transport along the direction perpendicular to the artificial interfaces of the SL reduces phonon heat conduction while maintaining or even enhancing the electron transport³. While some effort in experimental research was done^{8–13}, only a few theoretical works discuss the possible transport across such SL structures^{14,15}. While Park *et al.*¹⁴ discussed the effect of volume change on the in-plane thermoelectric transport properties of Bi_2Te_3 , Sb_2Te_3 and their related compound, Li *et al.*¹⁵ focussed on the calculation of the electronic structure for a $\text{Bi}_2\text{Te}_3/\text{Sb}_2\text{Te}_3$ -SL, stating changes of the mobility anisotropy estimated from effective masses.

Superlattices are anisotropic by definition and even the telluride bulk materials show intrinsic anisotropic structural and electronic properties. However, investigations of Venkatasubramanian *et al.* found a strong decrease for the mobility anisotropy and the thermoelectric properties for the $\text{Bi}_2\text{Te}_3/\text{Sb}_2\text{Te}_3$ -SL at certain periods. The reason for this behaviour is still on debate and could be related to strain effects which are induced by the epitaxial growth of the $\text{Bi}_2\text{Te}_3/\text{Sb}_2\text{Te}_3$ -SL. To extend previous works^{16–18} and to clarify the open question on the reduced anisotropy, we are going to discuss in this paper the anisotropic electronic transport in bulk Bi_2Te_3 and Sb_2Te_3 and the possible influence of strain in epitaxially grown SL on the TE properties.

For this purpose the paper will be organized as follows. In section II we introduce our first principle electronic structure calculations based on density functional theory and the semi-classical transport calculations based on the solution of the linearized Boltzmann equation. With this, we discuss the thermoelectric transport properties, that is electrical conductivity, thermopower and the related powerfactor, of unstrained Bi_2Te_3 and Sb_2Te_3 with a focus on their directional anisotropies. While in epitaxially grown $\text{Bi}_2\text{Te}_3/\text{Sb}_2\text{Te}_3$ -SL the atoms near the interfaces may be shifted from their bulk positions due to the lattice mismatch and the changed local environment, we modelled Bi_2Te_3 with the experimental lattice parameters and interatomic distances of Sb_2Te_3 , and vice versa. We assume that from these two limiting cases one could estimate the effect of the interface relaxation on the electronic and transport properties in $\text{Bi}_2\text{Te}_3/\text{Sb}_2\text{Te}_3$ -SL. With that structural data we first analyse in section III the anisotropic thermoelectric properties of the unstrained bulk systems, while in section IV a detailed view on the influence of strain, which may occur in $\text{Bi}_2\text{Te}_3/\text{Sb}_2\text{Te}_3$ -SL, on the electronic transport of these tellurides is given. Throughout the paper we quote Bi_2Te_3 (Sb_2Te_3) as strained, if it is considered in the lattice structure of Sb_2Te_3 (Bi_2Te_3). As in the SL p-type,

as well as n-type, transport was reported, we discuss the concentration dependence for both types of carriers on the transport properties.

II. METHODOLOGY

For both bismuth and antimony telluride we used the experimental lattice parameters and relaxed atomic positions¹⁹ as provided for the rhombohedral crystal structure with five atoms, i.e. one formula unit, per unit cell belonging to the space group $D_{3d}^5 (R\bar{3}m)$. The related layered hexagonal structure is composed out of three formula units and has the lattice parameters $a_{\text{BiTe}}^{\text{hex}} = 4.384\text{\AA}$, $c_{\text{BiTe}}^{\text{hex}} = 30.487\text{\AA}$, and $a_{\text{SbTe}}^{\text{hex}} = 4.264\text{\AA}$, $c_{\text{SbTe}}^{\text{hex}} = 30.458\text{\AA}$, for Bi_2Te_3 and Sb_2Te_3 , respectively. In fact, the main difference between the lattices of Bi_2Te_3 and Sb_2Te_3 is a decrease of the in-plane lattice constant with an accompanied decrease in cell volume. So, a change between the two lattice constants can be related to either compressive or tensile in-plane strain. This is very similar to the approach by Park *et al.*¹⁴, while omitting computational relaxation of internal atomic positions.

Our electronic structure calculations are performed in two steps. In a first step the detailed band structure of the strained and unstrained Bi_2Te_3 and Sb_2Te_3 was obtained by first principles density functional theory calculations (DFT), as implemented in the fully relativistic screened Korringa-Kohn-Rostoker Greens-function method (KKR)²⁰. Within this approach the DIRAC-equation is solved self-consistently and with that spin-orbit-coupling is included. Exchange and correlation effects were accounted for by the local density approximation (LDA) parametrized by Vosco, Wilk, and Nusair²¹. A detailed discussion on the influence of strain on the band structure topology of Bi_2Te_3 and Sb_2Te_3 is recently published²². With the well converged results from the first step we obtain the thermoelectric transport properties by solving the linearized Boltzmann equation in relaxation time approximation (RTA) within an in-house developed Boltzmann transport code^{23–25}. Boltzmann transport calculations for thermoelectrics have been carried out for quite a long time and show reliable results for metals^{26–28} as well as for wide- and narrow gap semiconductors^{25,29–32}. TE transport calculations for bulk Bi_2Te_3 ^{14,18,33,34} and Sb_2Te_3 ^{14,17,35} were presented before. Here the relaxation time τ is assumed to be constant with respect to wave vector k and energy on the scale of $k_B T$. This assumption is widely accepted for metals and highly doped semiconductors. Most of the presented results are in this high-doping regime. Within the RTA the transport distribution function $\mathcal{L}_{\perp,\parallel}^{(0)}(\mu, 0)$ (TDF)³⁶ and with this the generalized conductance mo-

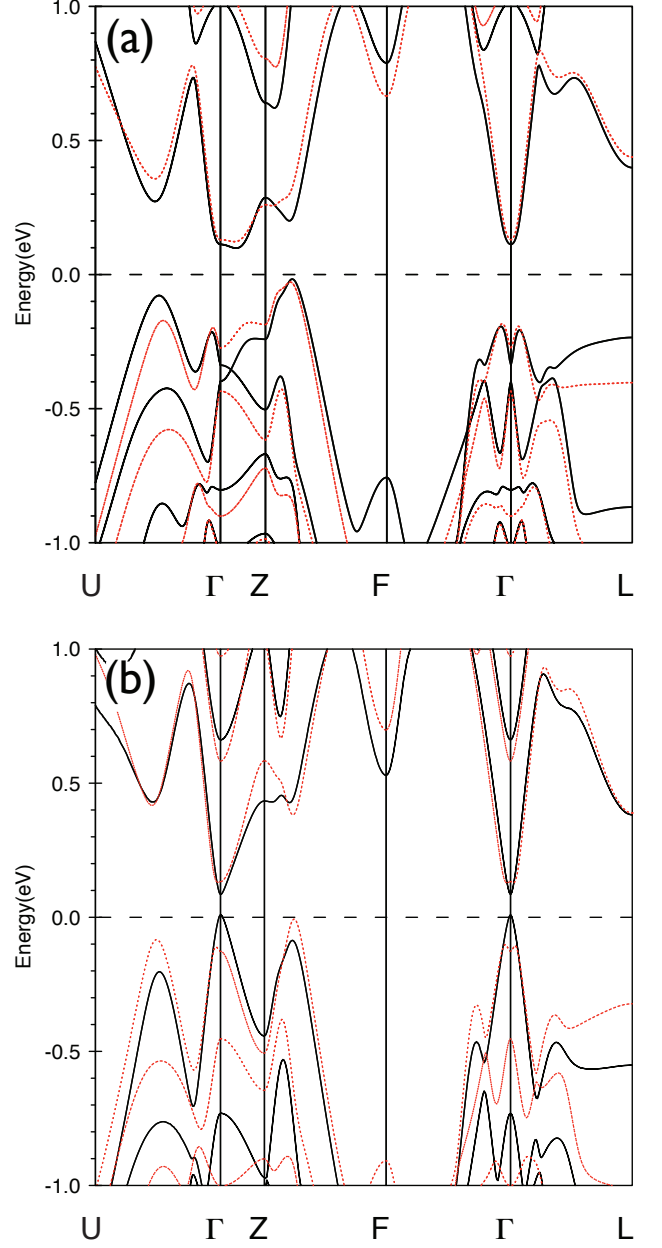


FIG. 1: (color online) Band structures of (a) Bi_2Te_3 and (b) Sb_2Te_3 along symmetry lines for both unstrained (black solid lines) and strained (red dashed lines) lattices. Energies are given relative to the valence band maximum.

ments $\mathcal{L}_{\perp,\parallel}^{(n)}(\mu, T)$ are defined as

$$\mathcal{L}_{\perp,\parallel}^{(n)}(\mu, T) = \frac{\tau_{\perp,\parallel}}{(2\pi)^3} \sum_{\nu} \int d^3k \left(v_{k,(\perp,\parallel)}^{\nu} \right)^2 (E_k^{\nu} - \mu)^n \left(-\frac{\partial f_{(\mu,T)}}{\partial E} \right)_{E=E_k^{\nu}}. \quad (2)$$

$v_{k,(\parallel)}, v_{k,(\perp)}^{\nu}$ denote the group velocities in the directions in the hexagonal basal plane and perpendicular to it,

respectively. Within here the group velocities were obtained as derivatives along the lines of the Blochl mesh in the whole Brillouin zone²². A detailed discussion on implications and difficulties on the numerical determination of the group velocities in highly anisotropic materials is currently published elsewhere³⁷. As can be seen straight forwardly, the electrical conductivity σ in- and cross-plane is then given by

$$\sigma_{\perp,\parallel} = 2e^2 \mathcal{L}_{\perp,\parallel}^{(0)}(\mu, T) \quad (3)$$

and the temperature- and doping-dependent thermopower states as

$$S_{\perp,\parallel} = \frac{1}{eT} \frac{\mathcal{L}_{\perp,\parallel}^{(1)}(\mu, T)}{\mathcal{L}_{\perp,\parallel}^{(0)}(\mu, T)} \quad (4)$$

for given chemical potential μ at temperature T and extrinsic carrier concentration N determined by an integration over the density of states $n(E)$

$$N = \int_{\mu-\Delta E}^{\text{VB}^{max}} dE n(E) [f_{(\mu,T)} - 1] + \int_{\text{CB}^{min}}^{\mu+\Delta E} dE n(E) f_{(\mu,T)}, \quad (5)$$

where CB^{min} is the conduction band minimum and VB^{max} is the valence band maximum. The energy range ΔE has to be taken sufficiently large to cover the tails of the FERMI-DIRAC distribution function $f_{(\mu,T)}$ and to ensure convergence of the integrals in eq. 2 and 5²⁵. The k-space integration of eq. 2 for a system with an intrinsic anisotropic texture is quite demanding. In previous publications^{22,37} we stated on the relevance of adaptive integration methods needed to reach convergence of the energy dependent TDF. Especially in regions close to the band edges the anisotropy of the TDF requires a high density of the k-mesh. Here, convergence tests for the transport properties showed that at least 150 000 k-points in the entire BZ had to be included for sufficient high doping rates ($N \geq 1 \times 10^{19} \text{ cm}^{-3}$), while for energies near the band edges even more than 56 million k-points were required to reach the analytical values for the conductivity anisotropies at the band edges⁵⁴. Within the RTA, from comparison of the calculated electrical conductivities (eq. 3) with experiment it is possible to conclude on the directional anisotropy of τ . For the thermopower S (eq. 4) the dependence of the TDF on the energy is essential. That is, not only the sloop of the TDF, moreover the overall functional behaviour of the TDF on the considered energy scale has to change to observe an impact on the thermopower. The calculations in this paper aim to cover band structure effects and not scattering specific impacts by an energy- and state-dependent relaxation time.

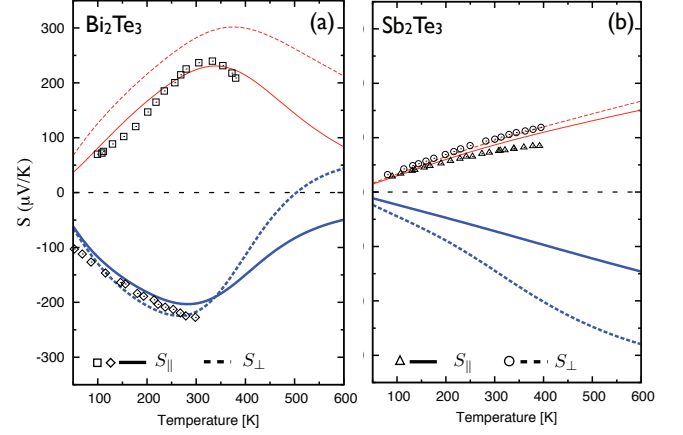


FIG. 2: (color online) Anisotropic thermopower for bulk (a) Bi_2Te_3 and (b) Sb_2Te_3 in their unstrained bulk lattice constants. Electron doping refers to the blue (thick) lines in the lower part of the figure, while red (thin) lines refer to hole doping and positive values of the thermopower. Solid lines show the in-plane part S_{\parallel} of the thermopower, while dashed lines show the cross-plane part S_{\perp} . The extrinsic charge carrier concentration of Bi_2Te_3 and Sb_2Te_3 was fixed to $N = 1 \times 10^{19} \text{ cm}^{-3}$ and $N = 1 \times 10^{20} \text{ cm}^{-3}$, respectively. Experimental data (squares, diamonds, circles, triangles) from Ref. 41–43 are given for comparison.

III. ANISOTROPIC THERMOELECTRIC PROPERTIES OF UNSTRAINED Bi_2Te_3 AND Sb_2Te_3

In order to understand the experimental findings on the in-plane and cross-plane transport of the $\text{Bi}_2\text{Te}_3/\text{Sb}_2\text{Te}_3$ -SL, in the following section the anisotropies of the electrical conductivity, the thermopower and the related powerfactor of bulk Bi_2Te_3 and Sb_2Te_3 are discussed. Even though the behaviour of Sb_2Te_3 is strongly p-type with a extrinsic carrier concentration of $N = 1 \dots 10 \times 10^{20} \text{ cm}^{-3}$,³⁸ we also discuss the related n-doped case, as in $\text{Bi}_2\text{Te}_3/\text{Sb}_2\text{Te}_3$ -SL n- as well as p-doping was reported. Bulk Bi_2Te_3 is known to be inherent electron conducting, while hole doping is experimentally achievable for bulk systems^{4,39–41}. Figure 2 shows the variation of the anisotropic thermopower for unstrained Bi_2Te_3 and Sb_2Te_3 in a wide temperature range. The extrinsic charge carrier concentration of Bi_2Te_3 and Sb_2Te_3 was fixed to $N = 1 \times 10^{19} \text{ cm}^{-3}$ and $N = 1 \times 10^{20} \text{ cm}^{-3}$, respectively. As a reference experimental values for both single crystalline materials at the same doping conditions are given and an excellent agreement can be stated. It is worth noting, that within eq. 4 the calculation of the thermopower is completely free of parameters. For Bi_2Te_3 the in-plane thermopower reaches a maximum of $S_{\parallel} \sim -200 \mu\text{V/K}$ at 300 K, while the maximum for the hole-doped case is shifted to slightly higher temperatures of 350 K with a maximum values of $S_{\parallel} \sim 225 \mu\text{V/K}$. We note, that the

temperature of the maximum is slightly overestimated. This might be caused by the missing temperature dependence of the energy gap, which was determined as $E_g = 105$ meV for unstrained Bi_2Te_3 . The anisotropy of the thermopower is more pronounced for the p-doped case. Here the cross-plane thermopower S_\perp is for the given doping always larger than the in-plane part S_\parallel . The anisotropy S_\parallel/S_\perp is about 0.64 at 100K, evolving to $S_\parallel/S_\perp \sim 0.79$ and $S_\parallel/S_\perp \sim 0.55$ at 300K and 500K, respectively. The sole available experimental data show no noticeable anisotropy for the thermopower in the hole-doped case⁴². For the electron-doped case the situation is more sophisticated. While upto 340K the overall anisotropy is rather small, with values $S_\parallel/S_\perp \sim 0.9$, a considerable decrease of S_\perp at higher temperatures leads to high values of S_\parallel/S_\perp for temperatures above 400K. This tendency could also be revealed by experiments^{44,45}. The crossing point of S_\parallel and S_\perp near room temperature could explain the fact of varying measured anisotropies for the thermopower at 300K. Here anisotropy ratios of $S_\parallel/S_\perp = 0.97 \dots 1.10$ were reported^{41,45}. The maximum peak of the thermopower near room temperature can be explained by the position of the chemical potential μ as a function of temperature at a fixed carrier concentration. For T much smaller than 300K the chemical potential is located in either the conduction- or valence band with the tails of the Fermi-Dirac-distribution in eq. 2 only playing a subsidiary role. For rising temperatures the chemical potential shifts towards the band edges and S maximizes. At these conditions the conduction is mainly unipolar. For higher temperatures the chemical potential shifts into the bandgap and conduction becomes bipolar leading to a reduced thermopower. For the case of Sb_2Te_3 , shown in fig. 2(b), the situation is different. Due to the ten times higher inherent doping and the smaller energy gap of $E_g = 90$ meV, the chemical potential is located deeply in the bands for the whole relevant temperature range. Therefore the functional behaviour can be understood in terms of the well known MOTT relation, where equation 4 qualitatively coincides with $S \propto T \cdot \frac{d \ln \sigma(E)}{dE} \big|_{E=\mu}$ for the thermopower in RTA⁴⁶. With increasing temperature the thermopower increases almost linearly, showing values of $S_\parallel \sim 87 \mu\text{V/K}$ and $S_\perp \sim -72 \mu\text{V/K}$ at 300K for p- and n-doping, respectively. The anisotropy of the thermopower for the hole-doped case is around $S_\parallel/S_\perp = 0.91$, almost temperature-independent and slightly underestimates the available experimental values^{47,48}. While for the electron-doped case the absolute values of the in-plane thermopower are comparable to those of the hole-doped case, the anisotropies are rather large. The anisotropy varies only weakly on temperature showing $S_\parallel/S_\perp = 0.48 \dots 0.52$ over the hole temperature range. While bulk Sb_2Te_3 states a strong p-character due to inherent defects, we note here again, that n-doping is available in heterostructures combining Bi_2Te_3 and Sb_2Te_3 ⁵.

A strongly enhanced cross-plane thermopower S_\perp could lead to a strongly enhanced powerfactor PF_\perp ,

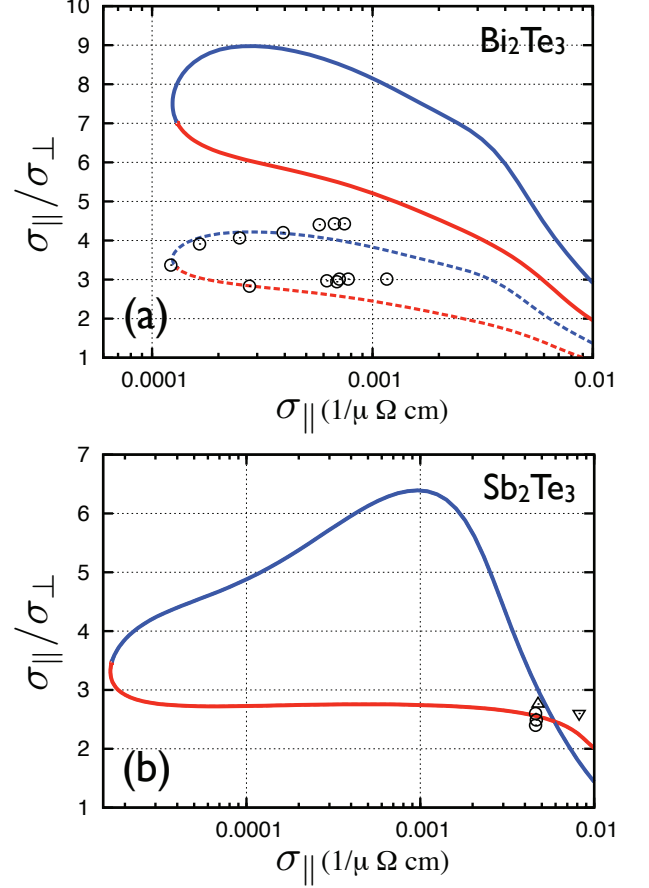


FIG. 3: (color online) Ratio $\sigma_\parallel / \sigma_\perp$ of the electrical conductivities at 300K for unstrained bulk (a) Bi_2Te_3 and (b) Sb_2Te_3 . Electron doping refers to blue lines, while red lines refer to hole doping. The dashed lines in panel (a) present the ratio obtained with an anisotropic relaxation time $\tau_{xx}/\tau_{zz} = 0.47$, while all other results are obtained with an isotropic relaxation time. Experimental data (circles and triangles) from Ref. 39,48,49 are given for comparison.

if the cross-plane electrical conductivity σ_\perp is maintained at the bulk value. For this purpose the anisotropy of the electrical conductivity in dependence on the in-plane conductivity σ_\parallel for unstrained Bi_2Te_3 and Sb_2Te_3 is shown in Figure 3. The temperature is fixed at 300K, blue and red lines refer to electron- and hole-doping, respectively. From comparison with experimental data⁵⁵, the in-plane relaxation time is determined to be $\tau_\parallel = 1.1 \times 10^{-14}$ s and $\tau_\parallel = 1.2 \times 10^{-14}$ s for Bi_2Te_3 and Sb_2Te_3 , respectively. With that we find strong anisotropies for the electrical conductivity $\sigma_\parallel/\sigma_\perp \gg 1$, clearly preferring the in-plane transport in both bulk tellurides. For the strongly suppressed cross-plane conduction p-type conduction is more favoured than n-type conduction. For Bi_2Te_3 the pure band structure effects (solid lines in Figure 3(a)) overestimate the measured anisotropy ratio³⁹ of the electrical conductivity. With an assumed anisotropy of

the relaxation time of $\tau_{\parallel}/\tau_{\perp} = 0.47$ the experimental values are reproduced very well. That means, scattering effects strongly affect the transport and electrons travelling along the basal plane direction are scattered stronger than electrons travelling perpendicular to the basal plane. The origin of this assumed anisotropy has to be examined by defect calculations and resulting microscopic transition probabilities and state dependent mean free path vectors. It is well known, that in Bi_2Te_3 mainly anti-site defects lead to the inherent conduction behaviour^{38,45,50}. We have shown elsewhere³⁷, that the integration of the transport integrals eq. 2 in anisotropic k-space requires large numeric effort. Tiny regions in k-space close to the band gap have to be scanned very carefully and the texture in k-space has a drastic influence on the obtained anisotropy values, if integrals are not converged with respect to the k-point density. As shown, some integration methods tend for the given k-space symmetry to underestimate the ratio $\sigma_{\parallel}/\sigma_{\perp}$ in a systematic manner and therefore would shift anisotropy closer to the experimental observed values, without representing the real band structure effects. For unstrained Bi_2Te_3 the electrical conductivity anisotropy is highest for low values of σ_{\parallel} , i.e. small amounts of doping and bipolar conduction. For larger charge carrier concentrations, i.e. the chemical potential shifts deeper into either conduction or valence band, the in-plane conductivity σ_{\parallel} increases and the ratio $\sigma_{\parallel}/\sigma_{\perp}$ decreases. Values for $\sigma_{\parallel}/\sigma_{\perp}$ will lower from 7 to 2 for p-type conduction and 9 to 3 for n-type conduction. However, cross-plane electrical transport is always more suppressed for n-type carrier conduction, which also holds for unstrained Sb_2Te_3 . As shown in Figure 3(b) $\sigma_{\parallel}/\sigma_{\perp}$ is almost doping independent for hole-doping, showing an anisotropy of around 2.7 in very good agreement with experiment (circle and triangles in fig. 3 from Ref. 47–49). In this case no anisotropic relaxation times had to be assumed. For electron doping the ratio $\sigma_{\parallel}/\sigma_{\perp}$ is clearly higher, evolving values of 3.5 to 6 for rising in-plane conductivity. The dependence of the anisotropy ratio on the applied doping, i.e. changing σ_{\parallel} , can be directly linked to the functional behaviour of the TDF near band edges, which is crucially influenced by the topology of the band structure²².

IV. ANISOTROPIC THERMOELECTRIC PROPERTIES OF STRAINED Bi_2Te_3 AND Sb_2Te_3

Before the influence of in-plane strain on the resulting powerfactor will be discussed, we will first note on the strain induced changes of the components electrical conductivity and thermopower. In Figure 4 the anisotropy of the electrical conductivity $\sigma_{\parallel}/\sigma_{\perp}$ is shown for both Bi_2Te_3 in the lattice constant of Sb_2Te_3 , i.e. under biaxial compressive in-plane strain (Figure 4(a)), and Sb_2Te_3 in the lattice constant of Bi_2Te_3 , i.e. under biaxial tensile in-plane strain (Figure 4(b)).

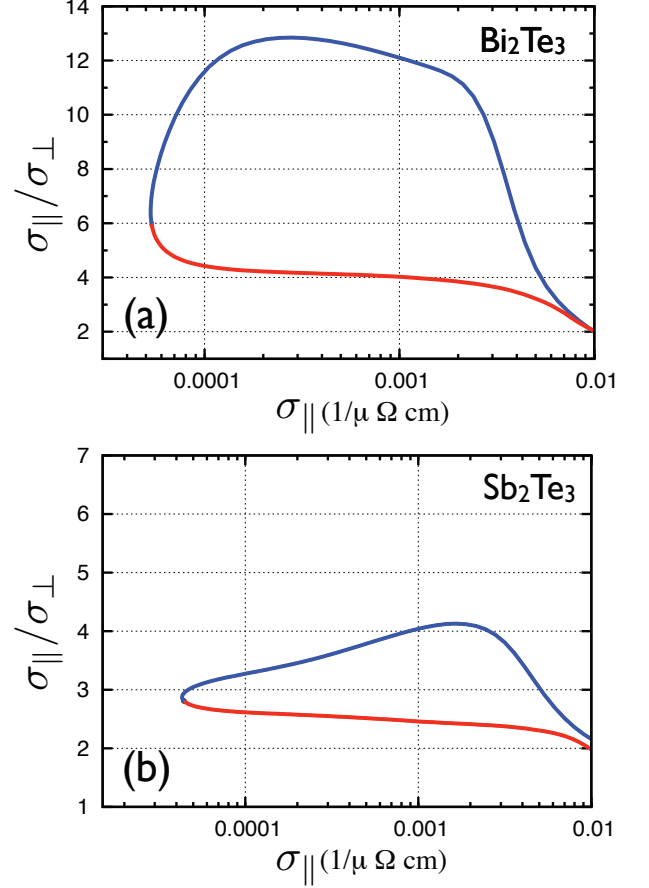


FIG. 4: (color online) Conductivity ratio $\sigma_{\parallel}/\sigma_{\perp}$ of the electrical conductivities at 300K for bulk (a) Bi_2Te_3 in the Sb_2Te_3 structure and (b) Sb_2Te_3 in the Bi_2Te_3 structure. Electron doping refers to blue lines, while red lines refer to hole doping. Isotropic relaxation times of $\tau = 1.1 \times 10^{-14}$ s and $\tau = 1.2 \times 10^{-14}$ s for σ_{\parallel} and σ_{\perp} are assumed for Bi_2Te_3 and Sb_2Te_3 , respectively.

For Bi_2Te_3 the compressive in-plane strain causes an increase of the band gap by around 23% yielding $E_g = 129$ meV. While the anisotropy $\sigma_{\parallel}/\sigma_{\perp}$ for hole doping (red lines in fig. 4(a)) decreases to around 4 and is almost constant under varying doping level, the ratio considerably raises under electron doping to values up to 13 for $\sigma_{\parallel} \sim 100 \dots 1000 (\Omega \text{ cm})^{-1}$, corresponding to electron charge carrier concentrations of $N = 3 \dots 30 \times 10^{19} \text{ cm}^{-3}$. This concludes, that the cross-plane electrical conductivity of Bi_2Te_3 under compressive in-plane strain will be noticeably enhanced for p-doping, but drastically suppressed for n-doping. Such a compressive in-plane strain could be introduced by either a substrate with smaller in-plane lattice constant, e.g. GaAs-[111] with $a = 3.997 \text{ \AA}$, or a considerable amount of Sb_2Te_3 in the $\text{Bi}_2\text{Te}_3/\text{Sb}_2\text{Te}_3$ -SL. For tensile in-plane strained Sb_2Te_3 the impact on the electrical conductivity ratio $\sigma_{\parallel}/\sigma_{\perp}$ is less prominent. As shown in figure 4(b) at

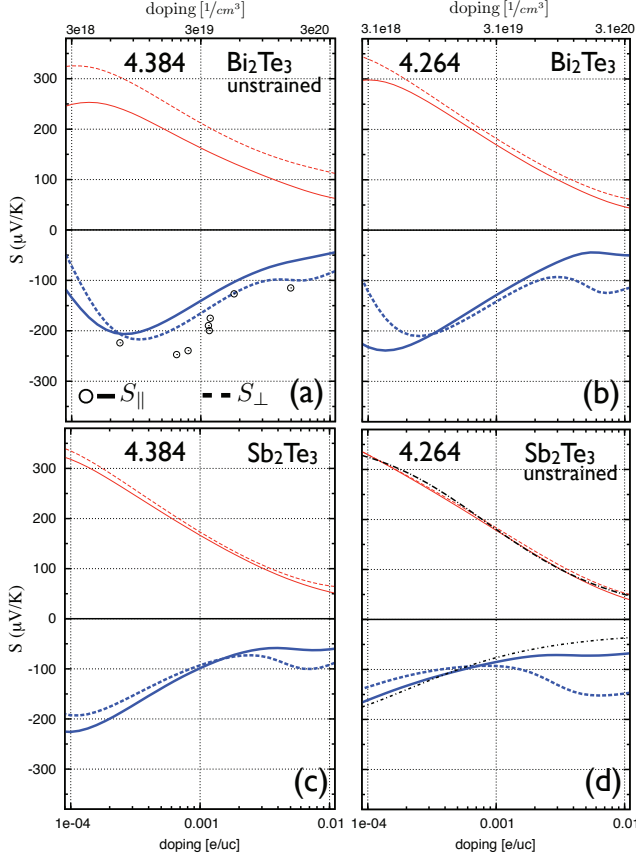


FIG. 5: (color online) In-plane (solid lines) and cross-plane (dashed lines) doping-dependent thermopower at 300K for (a) Bi₂Te₃ in the Bi₂Te₃ structure, (b) Bi₂Te₃ in the Sb₂Te₃ structure, (c) Sb₂Te₃ in the Bi₂Te₃ structure and (d) Sb₂Te₃ in the Sb₂Te₃ structure. Electron (hole) doping is presented as blue thick (red thin) line. The black (dashed-dotted) line in panel (d) shows the PISARENKO-dependence of the thermopower expected for parabolic bands. Experimental data (circles) from Ref. 51 is given for comparison. The charge carrier concentration is stated in units of e/uc (1/cm³) at the bottom (top) x-axis.

hole doping $\sigma_{\parallel}/\sigma_{\perp} \sim 2.5$ is only marginally altered compared to the unstrained case (comp. fig. 3(b)). Meanwhile $\sigma_{\parallel}/\sigma_{\perp}$ decreases noticeably for n-type doping yielding about 3 at low σ_{\parallel} and low electron charge carrier concentrations, and slightly higher values of $\sigma_{\parallel}/\sigma_{\perp} \sim 4$ for higher doping. Overall, the tensile strain reduces the electrical conductivity anisotropy by a factor of about 1.5, directly leading to an enhanced electrical conductivity along the z-axis of single crystal Sb₂Te₃. We note, that tensile in-plane strain opens the gap remarkably by around 56% compared to the unstrained case to a value of $E_g = 140$ meV. Furthermore, such tensile strain could be incorporated by using either a substrate with larger in-plane lattice constant, e.g. PbTe-[111] with $a = 4.567$ Å, or a higher fractional amount of Bi₂Te₃ in Bi₂Te₃/Sb₂Te₃-SL. In Figure 5(a), (d) ((b),

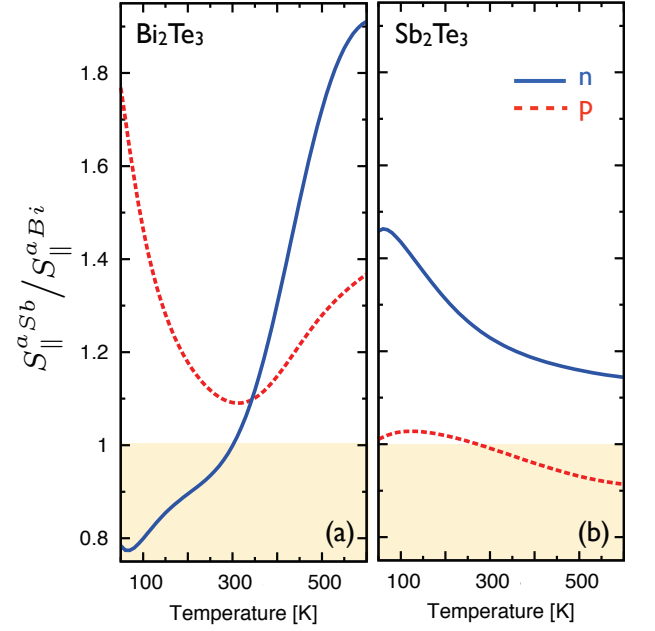


FIG. 6: (color online) Change of the in-plane thermopower S_{\parallel} under applied strain for (a) Bi₂Te₃ and (b) Sb₂Te₃. Given is the ratio of S_{\parallel} in the "smaller" lattice of Sb₂Te₃ divided by S_{\parallel} in the "larger" lattice of Bi₂Te₃. The doping was fixed to $N = 1 \times 10^{19}$ cm⁻³ for Bi₂Te₃ and $N = 1 \times 10^{20}$ cm⁻³ for Sb₂Te₃. Solid blue (dashed red) lines refer to electron (hole) doping, respectively.

(c) the doping dependent anisotropic thermopower of unstrained (strained) Bi₂Te₃ and Sb₂Te₃ at room temperature is shown, respectively. Blue thick (red thin) solid lines represent the in-plane thermopower S_{\parallel} under electron doping (hole doping). The corresponding cross-plane thermopower S_{\perp} is shown as a dashed line. The black dashed-dotted lines in fig. 5(d) emphasize the expected doping dependent behaviour of the thermopower for parabolic bands, following the PISARENKO-relation⁵². For both tellurides we found, that the anisotropy of the thermopower shows a weak dependence on the strain state. However, for strained Bi₂Te₃ (see fig. 5(b)) the thermopower anisotropy under hole doping almost vanishes, leading to $S_{\parallel} \sim S_{\perp}$. It is worth noting, that the anisotropy of the thermopower is less pronounced for hole doping, than for electron doping for Bi₂Te₃ and Sb₂Te₃ in both strain states. As shown by the black dashed-dotted lines in fig. 5(d), the dependency of the thermopower on the charge carrier concentration differs from the PISARENKO-relation⁵² under sufficient high electron doping. This indicates, that the nonparabolicity of the energy bands has a noticeable impact in the investigated doping regime and should not be omitted by applying parabolic band models.

Actually, changes for the absolute values of the thermopower can be found for both telluride systems under applied strain. In fig. 6 the relative change for the in-

plane component S_{\parallel} for both tellurides under in-plane strain is given. To compare the changes with the lattice constant, we relate the in-plane thermopower S_{\parallel} at the smaller lattice constant a_{SbTe} to the value at the larger lattice constant a_{BiTe} for both compounds. The doping was fixed to $N = 1 \times 10^{19} \text{ cm}^{-3}$ for Bi_2Te_3 and $N = 1 \times 10^{20} \text{ cm}^{-3}$ for Sb_2Te_3 as done for fig. 2. Figure 6(a) shows, that in the relevant temperature range between 350K and 450K the thermopower increases for Bi_2Te_3 under compressive strain for both p and n doping by about 15-20%. For Sb_2Te_3 a decrease is expected under tensile strain at electron doping and nearly no change under hole doping (see Figure 6(b)). With nearly all values above 1 for Bi_2Te_3 , as well as for Sb_2Te_3 , it is obvious, that higher values of the thermopower require a smaller unit cell volume. One can expect, that the volume decrease causes a larger density of states and thus a shift of the chemical potential towards the corresponding band edge, connected with an increase of the thermopower S . However Park *et al.*¹⁴ reported an unexpected increase of 16% for the in-plane thermopower S_{\parallel} of Sb_2Te_3 under p-doping ($T=300\text{K}$, $N = 1.32 \times 10^{19} \text{ cm}^{-3}$) if the material is strained into the Bi_2Te_3 structure. In the same doping and temperature regime we find a slight decrease of 4% for S_{\parallel} .

Comprising the statements on the electrical conductivity and the thermopower, the related powerfactor for both tellurides in their bulk lattice and in the strained state are compared in fig. 7. It is well known, that optimizing the powerfactor σS^2 of a thermoelectric always involves a compromise on the electrical conductivity σ and the thermopower S ⁵³. Due to the interdependence of σ and S it is not advisable to optimize the powerfactor by optimizing its parts. In Figure 7(a) and (d) the doping dependent anisotropic powerfactor of unstrained Bi_2Te_3 and Sb_2Te_3 at room temperature is shown, respectively. Blue thick (red thin) solid lines represent the in-plane powerfactor PF_{\parallel} under electron doping (hole doping). The corresponding cross-plane powerfactor PF_{\perp} is shown as a dashed line. Under p-doping both unstrained materials show a maximum powerfactor near carrier concentrations of $N \sim 4 \times 10^{19} \text{ cm}^{-3}$. Absolute values of $35 \mu\text{W}/\text{cmK}^2$ and $33 \mu\text{W}/\text{cmK}^2$ were found for unstrained Bi_2Te_3 and Sb_2Te_3 , respectively, which is in good agreement to experimental and theoretical findings^{9,14,51}. Under electron doping the absolute values of PF_{\parallel} (thick blue lines in fig. 7) were found to be distinctly smaller. This is due to smaller absolute values of the thermopower for electron doping compared to hole doping (see Figure 2) and apparently smaller in-plane electrical conductivities σ_{\parallel} at fixed carrier concentrations. As a result, a powerfactor of $18 \mu\text{W}/\text{cmK}^2$ and $8 \mu\text{W}/\text{cmK}^2$ can be stated for unstrained Bi_2Te_3 and Sb_2Te_3 , respectively, under optimal electron doping. We notice, that the powerfactor for unstrained Sb_2Te_3 is monotonically increasing for electron carrier concentrations of $N \sim 6 \dots 30 \times 10^{19} \text{ cm}^{-3}$. This behaviour can be linked to a deviation of S_{\parallel} from the PISARENKO-

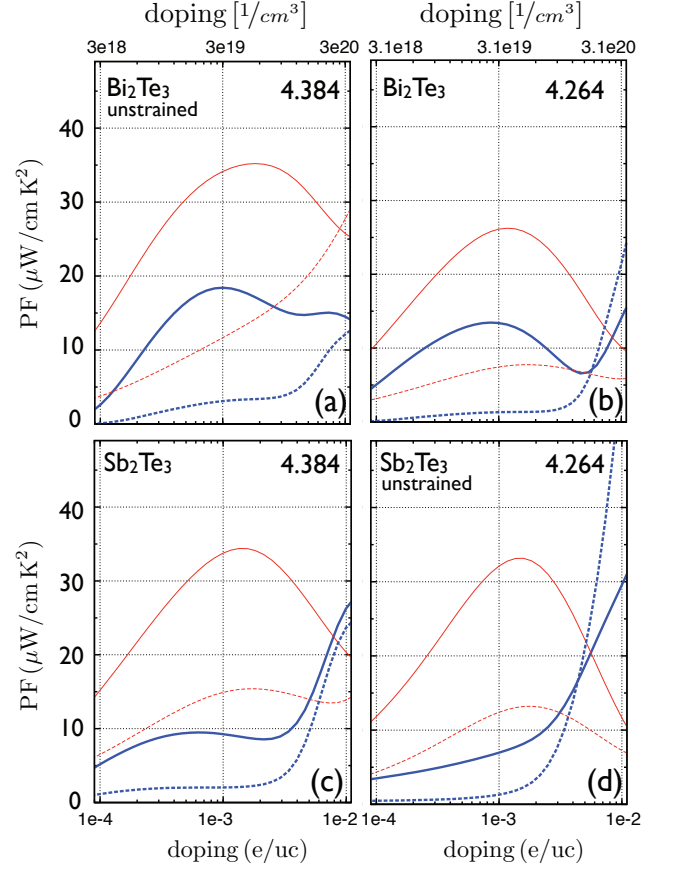


FIG. 7: (color online) In-plane (solid lines) and cross-plane (dashed lines) doping-dependent powerfactor at 300K for (a) Bi_2Te_3 in the Bi_2Te_3 structure, (b) Bi_2Te_3 in the Sb_2Te_3 structure, (c) Sb_2Te_3 in the Bi_2Te_3 structure and (d) Sb_2Te_3 in the Sb_2Te_3 structure. Electron (hole) doping is presented as blue thick (red thin) line. The charge carrier concentration is stated in units of e/uc ($1/\text{cm}^3$) at the bottom (top) x-axis.

relation under electron doping. While it is expected, that the thermopower will decrease for increasing carrier concentration, S_{\parallel} was found to be almost constant in an electron doping range of $N \sim 6 \dots 30 \times 10^{19} \text{ cm}^{-3}$ (see fig. 5(d)). For the investigated electron doping range of $N \sim 6 \dots 30 \times 10^{19} \text{ cm}^{-3}$ the chemical potential μ at 300K is located around $300 \dots 450 \text{ meV}$ above the VBM. As can be seen from the band structure for unstrained Sb_2Te_3 in fig. 1(b) (black, solid lines) flat non-parabolic bands near the high symmetry point Z dominate in this energy region and most likely lead to an increased thermopower. This feature is more pronounced for unstrained Sb_2Te_3 , than for strained Sb_2Te_3 (red, dashed lines in fig. 1(b)). Similar statements can be done for strained and unstrained Bi_2Te_3 (see fig. 1(a)). We note, even though this picture is convincing, it is difficult to link such specific anomalies to the band structure on high symmetry lines, as the underlying TDF is an integral quantity over all occupied

states in the BZ.

Under applied in-plane compressive strain for Bi_2Te_3 (ref. Figure 7(b)) and tensile strain for Sb_2Te_3 (ref. Figure 7(c)) the obtained changes in the powerfactor are noticeable different for both tellurides. While for Bi_2Te_3 a decrease of the maximal powerfactor PF_{\parallel} of about 27% and 23% for n-doping and p-doping was found, the strain shows nearly no influence on the powerfactor for Sb_2Te_3 . At a carrier concentration of about $N \sim 3 \times 10^{19} \text{ cm}^{-3}$ the decrease in PF_{\parallel} for Bi_2Te_3 is about 17% and 28% for n- and p-doping, respectively, while in the work of Park *et al.*¹⁴ a slight increase of PF_{\parallel} under strain and hole doping is reported. Obviously this tendency has to be understood by analyzing the constituent parts σ_{\parallel} and S_{\parallel} . For compressively strained Bi_2Te_3 at a hole carrier concentration of about $N \sim 3 \times 10^{19} \text{ cm}^{-3}$ the electrical conductivity decreases by about 39% to $330 (\Omega \text{ cm s})^{-1}$. At the same time S_{\parallel} increases by about 9%, as shown in Figure 6(a). This results in the overall decrease of about 28% for PF_{\parallel} . Under electron doping of $N \sim 3 \times 10^{19} \text{ cm}^{-3}$ no influence of strain could be found for S_{\parallel} at room temperature (see solid blue lines in Figure 6(a)). Thus, the decrease of PF_{\parallel} under electron doping can be largely related to a decrease of the electrical conductivity under applied compressive strain. By detailed evaluation of the effective mass eigenvalues and eigenvectors we found a decrease of about 15% for the in-plane electrical conductivity of Bi_2Te_3 under applied strain in the low-temperature and low-doping limit^{22,37}. The discussion can be made in the same manner for Sb_2Te_3 ^{22,37}. The fact, that strain-induced effects in σ and S tend to compensate each other was already reported for the case of silicon²⁵.

As mentioned before (summarized in fig. 3 and fig. 4), we found a strong anisotropy in the electrical conductivity with $\sigma_{\parallel}/\sigma_{\perp} \gg 1$. The clearly preferred in-plane transport in both bulk tellurides is also reflected in the cross-plane powerfactor PF_{\perp} (dashed lines in Figure 7), which is clearly suppressed for all strain states. It is obvious that PF_{\perp} is more suppressed for electron-, than for hole-doping.

Nonetheless, we want to include experimental findings for the thermal conductivity to our calculations, to give an estimation for the figure of merit ZT in-plane and cross-plane. In Ref. 49 $\kappa_{\parallel} = 2.2 \text{ W/m K}$, $\kappa_{\perp} = 1.0 \text{ W/m K}$, and $\kappa_{\parallel} = 7.5 \text{ W/m K}$, $\kappa_{\perp} = 1.6 \text{ W/m K}$ for unstrained Bi_2Te_3 and Sb_2Te_3 are given, respectively. With this we find maximal values for the figure of merit at room temperature and optimal hole doping of $ZT_{\parallel} \sim 0.48$ and $ZT_{\perp} \sim 0.41$ for unstrained Bi_2Te_3 and $ZT_{\parallel} \sim 0.13$

and $ZT_{\perp} \sim 0.23$ for unstrained Sb_2Te_3 . We note, that the figure of merit ZT maximizes at slightly lower carrier concentration than the powerfactor σS^2 shown in fig. 7. This can be linked directly to an increasing electronic part of the thermal conductivity κ_{el} with increasing carrier concentration^{25,53}.

V. CONCLUSION

In the present paper the influence of in-plane strain on the thermoelectric transport properties of Bi_2Te_3 and Sb_2Te_3 is investigated. A focussed view on the influence of strain on the anisotropy of the electrical conductivity σ , thermopower S and the related powerfactor σS^2 could help to understand in-plane and cross-plane thermoelectric transport in nanostructured $\text{Bi}_2\text{Te}_3/\text{Sb}_2\text{Te}_3$ -superlattices. Based on detailed *ab initio* calculations we focussed mainly on band structure effects and their influence on the thermoelectric transport. For both tellurides no reasonable decrease of the anisotropy for σ and S could be found under strain, while in principle the anisotropy for σ and S is more pronounced under electron doping, than at hole doping. Thus a favoured thermoelectric transport along the z-direction of $\text{Bi}_2\text{Te}_3/\text{Sb}_2\text{Te}_3$ -heterostructures due to superlattice-induced in-plane strain effects can be ruled out and a clear preference of p-type thermoelectric transport can be stated for Bi_2Te_3 and Sb_2Te_3 and their related epitaxial heterostructures. The absolute value of the in-plane thermopower S_{\parallel} was increased under reduced cell volume, which is in contrast to recent findings by Park *et al.*¹⁴.

We found, that even if thermopower or electrical conductivity are enhanced or decreased via applied strain, they tend to compensate each other suppressing more distinct changes of the powerfactor under strain. We found the thermoelectrically optimal doping to be in the range of $N \sim 3 \dots 6 \times 10^{19} \text{ cm}^{-3}$ for all considered systems. Our assumption of an anisotropic relaxation time for Bi_2Te_3 states that already in the single crystalline system strong anisotropic scattering effects should play a role.

Acknowledgments

This work was supported by the Deutsche Forschungsgemeinschaft, SPP 1386 ‘Nanostrukturierte Thermoelektrika: Theorie, Modellsysteme und kontrollierte Synthese’. N. F. Hinsche is member of the International Max Planck Research School for Science and Technology of Nanostructures.

* Electronic address: nicki.hinsche@physik.uni-halle.de

¹ B. Sales, Science **295**, 1248 (2002).

² A. Majumdar, Science **303**, 777 (2004).

³ H. Böttner, G. Chen, and R. Venkatasubramanian, MRS Bulletin **31**, 211 (2006).

⁴ H. Goldsmid, A. Sheard, and D. Wright, British Journal

- of Applied Physics **9**, 365 (1958).
- ⁵ R. Venkatasubramanian, E. Siivola, and T. Colpitts, Nature **413**, 597 (2001).
 - ⁶ R. Venkatasubramanian, T. Colpitts, B. O'Quinn, S. Liu, N. El-Masry, and M. Lamvik, Applied Physics Letters **75**, 1104 (1999).
 - ⁷ R. Venkatasubramanian, Phys. Rev. B **61**, 3091 (2000).
 - ⁸ H. Beyer, J. Nurnus, H. Böttner, A. Lambrecht, E. Wagner, and G. Bauer, Physica E: Low-dimensional Systems and Nanostructures **13**, 965 (2002).
 - ⁹ H. Böttner, J. Nurnus, A. Gavrikov, and G. Kuhner, Journal of Microelectromechanical Systems **13**, 414 (2004).
 - ¹⁰ J. König, M. Winkler, S. Buller, W. Bensch, U. Schürmann, L. Kienle, and H. Böttner, Journal of electronic Materials **40**, 1266 (2011).
 - ¹¹ C.-N. Liao, C.-Y. Chang, and H.-S. Chu, Journal of Applied Physics **107**, 066103 (2010).
 - ¹² N. Peranio, O. Eibl, and J. Nurnus, Journal of Applied Physics **100**, 114306 (2006).
 - ¹³ M. N. Touzelbaev, P. Zhou, R. Venkatasubramanian, and K. E. Goodson, Journal of Applied Physics **90**, 763 (2001).
 - ¹⁴ M. S. Park, J.-H. Song, J. E. Medvedeva, M. Kim, I. G. Kim, and A. J. Freeman, Phys. Rev. B **81**, 155211 (2010).
 - ¹⁵ H. Li, D. Bile, and S. D. Mahanti, Mat. Res. Soc. Symp. Proc. **793**, 837 (2004).
 - ¹⁶ T. Scheidemantel, C. Ambrosch-Draxl, T. Thonhauser, J. Badding, and J. Sofo, Physical Review B **68**, 125210 (2003).
 - ¹⁷ T. Thonhauser, T. Scheidemantel, J. Sofo, J. Badding, and G. Mahan, Physical Review B **68**, 085201 (2003).
 - ¹⁸ B.-L. Huang and M. Kaviani, Phys. Rev. B **77**, 125209 (2008).
 - ¹⁹ Landolt-Börnstein New Series, group III/41C (Springer Verlag, Berlin, 1998).
 - ²⁰ M. Gradhand, M. Czerner, D. V. Fedorov, P. Zahn, B. Y. Yavorsky, L. Szunyogh, and I. Mertig, Phys. Rev. B **80**, 224413 (2009).
 - ²¹ S. H. Vosko and L. Wilk, Phys. Rev. B **22**, 3812 (1980).
 - ²² B. Yu. Yavorsky, N. F. Hinsche, I. Mertig and P. Zahn, arXiv:1109.0186 (2011).
 - ²³ I. Mertig, Reports on Progress in Physics **62**, 237 (1999).
 - ²⁴ P. Zahn, I. Mertig, M. Richter, and H. Eschrig, Phys. Rev. Lett. **75**, 2996 (1995).
 - ²⁵ N. F. Hinsche, I. Mertig, and P. Zahn, J. Phys.: Condens. Matter **23**, 295502 (2011).
 - ²⁶ T. Vojta, I. Mertig, and R. Zeller, Phys. Rev. B **46** (1992).
 - ²⁷ J. Yang, H. Li, T. Wu, and W. Zhang, Advanced Functional Materials **18**, 2880 (2008).
 - ²⁸ J. Barth, G. Fecher, B. Balke, S. Ouardi, T. Graf, C. Felser, A. Shkabko, A. Weidenkaff, P. Klaer, and H. Elmers, Physical Review B **81**, 064404 (2010).
 - ²⁹ D. J. Singh, Physical Review B **81**, 195217 (2010).
 - ³⁰ D. Parker and D. J. Singh, Physical Review B **82**, 035204 (2010).
 - ³¹ A. May, D. J. Singh, and G. J. Snyder, Physical Review B **79**, 153101 (2009).
 - ³² M.-S. Lee, F. Poudeu, and S. Mahanti, Physical Review B **83**, 085204 (2011).
 - ³³ S. Lee and P. von Allmen, Applied Physics Letters **88**, 022107 (2006).
 - ³⁴ M. Situmorang and H. Goldsmid, physica status solidi (b) **134**, K83 (1986).
 - ³⁵ T. Thonhauser, Solid State Communications **129**, 249 (2004).
 - ³⁶ G. Mahan and J. Sofo, Proceedings of the National Academy of Sciences **93**, 7436 (1996).
 - ³⁷ P. Zahn, B. Yu. Yavorsky, N. F. Hinsche and I. Mertig, arXiv:1108.0023 (2011).
 - ³⁸ D. M. Rowe, ed., CRC handbook of thermoelectrics (CRC Press London, 1995).
 - ³⁹ R. Delves, A. Bowley, and D. Hazelden, Proceedings of the Phys. Society **78**, 838 (1961).
 - ⁴⁰ H. Jeon, H. Ha, D. Hyun, and J. Shim, Journal of Physics and Chemistry of Solids **52**, 579 (1991).
 - ⁴¹ H. Kaibe, Journal of Physics and Chemistry of Solids **50**, 945 (1989).
 - ⁴² M. Stordeur and W. Kühnberger, physica status solidi (b) **69**, 377 (1975).
 - ⁴³ M. Stordeur and W. Heiliger, physica status solidi (b) **78**, K103 (1976).
 - ⁴⁴ M. Zhitinskaya, V. Kaidanov, and V. Kondratev, Soviet Physics Semiconductors **10**, 1300 (1976).
 - ⁴⁵ E. Müller, Bandstruktur und Ladungsträgerstreuung in p-leitenden (B) (VDI Verlag, Düsseldorf, 1998).
 - ⁴⁶ M. Cutler and N. Mott, Phys. Rev. **181**, 1336 (1969).
 - ⁴⁷ G. Simon and W. Eichler, phys. stat. sol. (b) **103**, 289 (1981).
 - ⁴⁸ H. Langhammer, M. Stordeur, H. Sobotta, and V. Riede, physica status solidi (b) **109**, 673 (1982).
 - ⁴⁹ A. Jacquot, N. Farag, M. Jaegle, M. Bobeth, J. Schmidt, D. Ebling, and H. Böttner, Journal of Electronic Materials **39**, 1861 (2010).
 - ⁵⁰ S. Cho, Y. Kim, A. Divenere, G. K. Wong, J. B. Ketterson, and J. R. Meyer, Applied Physics Letters **75**, 1401 (1999).
 - ⁵¹ J. Nurnus, Ph.D. thesis, Albert-Ludwigs-Universität Freiburg (2001).
 - ⁵² A. F. Ioffe, Physics of Semiconductors (Academic, New York, 1960).
 - ⁵³ G. J. Snyder and E. Toberer, Nature Materials **7**, 105 (2008).
 - ⁵⁴ The analytical value of the ratio $\sigma_{\parallel} / \sigma_{\perp}$ at the band edges was obtained by scanning the energy landscape near the conduction band minimum and valence band maximum fitting the dispersion relation in terms of an effective mass tensor. A detailed description is given in a recent publication by Ref. 22
 - ⁵⁵ The calculated dependencies of the electrical conductivity on the thermopower and the electrical conductivity on the applied doping were matched to fit experiments from Ref. 4,39,48.